Dropwise deposition and wetting of nanoparticle suspensions

Mathias Dietzel [*], Nicole R. Bieri, Dimos Poulikakos [1]

Laboratory of Thermodynamics in Emerging Technologies, Institute of Energy Technology, Department of Mechanical and Process Engineering, ETH Zurich, CH-8092 Zurich, Switzerland

Abstract

The wetting and spreading behavior of micron-sized colloidal nanoparticle suspension ('nanoink') droplets upon deposition on a flat substrate is investigated experimentally and numerically and compared to the behavior of the pure liquid solvent. Toluene containing gold particles is used as a reference working liquid, deposited either on a copper or a glass substrate. The experiments undertaken with a high-speed camera record the dynamic impact and spreading process and the results are used to calibrate a numerical model based on the Navier–Stokes equations in Lagrangian coordinates. The model accounts for wetting and the motion of a representative number of computational particles according to the relevant form of Newton's second law. The presence of the particles reduces spreading up to about 30%. The simulation using the particle model suggests that recirculation flow patterns during oscillatory recoiling phases lead to a particle pre-structuring in the vicinity of the substrate, providing an additional mechanism for the development of the characteristic trough shape encountered during the drying of printed colloidal suspension droplets.
© 2007 Elsevier Inc. All rights reserved.

Keywords: Nanoparticle colloidal suspension; Nanoinks; Wetting; Spreading; Impact

1. Introduction

Innovative small-scale manufacturing methods take advantage of the unique thermophysical properties of ultrafine particles in the nanometer range (Fuller et al., 2002; Bieri et al., 2003). These particles are commonly dispersed in a volatile carrier liquid ('nanoink') to use transport devices subject to more common engineering length scales such as drop-on-demand ink jet heads. The physical phenomena during the combined deposition, wetting/dewetting and evaporation of colloidal liquid films and droplets are complex, albeit practically omnipresent in nature and technology. Deegan et al. (1997) have identified the mechanism leading to ring formation from dried liquid coffee drops. On the technical side, Sun and Walker (2002)

investigated the two-dimensional self-assembly of latex particles on surfaces with squared-patterned rims and (Chung et al., 2003) observed that evaporation, Marangoni and wetting effects have considerable influence on the microstructures formed by coalesced nanoparticles after printing colloidal ink droplets on a substrate and applying heat to evaporate the carrier liquid.

For low heat fluxes where the temperature distribution in the droplet can be assumed to be spatially uniform (small Biot numbers), the following drying stages can be distinguished: initial heating and evaporation, quasi-equilibrium evaporation, crust formation at the free surface, boiling with the occurrence of arbitrary crust cracking through the evaporation pressure of the still enclosed liquid and finally porous particle drying (Nesic and Vodnik, 1991). Heating through the absorption of irradiated laser light usually coincides with a localized variation of the temperature dependent surface tension (thermal Marangoni effect), leading to Marangoni-Bénard cells. Local changes in particle surface concentration can induce destillo-

---
[*] Corresponding author. Tel.: +1 626 696 5196; fax: +41 44 63 21176.
E-mail addresses: mathias.dietzel@alumni.ethz.ch (M. Dietzel), poulikakos@ltnt.iet.mavt.ethz.ch (D. Poulikakos).
[1] Tel.: +41 44 63 22039; fax: +41 44 63 21176.

Nomenclature

Latin symbols

c	particle concentration [–]
c_s	speed of sound [m/s]
d_0	droplet diameter [m]
d_p	particle diameter [m]
Fr	Froude number [–]
g	gravity [m/s^2]
$H, \overline{H}$	curvature [1/m] [–]
H_a	Hamaker constant [J]
k_B	Boltzmann constant [J/K]
M	Mach number [–]
m	mass [kg]
n	absorption site number [–]
$\boldsymbol{n}$	normal vector [–]
p, P	pressure [Pa] [–]
r, R	radial coordinate [m] [–]
R_{CL}	contact line radius [–]
Re	Reynolds number [–]
s, S	arc length [m] [–]
$\tilde{S}$	spreading parameter [N/m]
t	time [s]
$\boldsymbol{t}$	tangential vector [–]
T	temperature [K, °C]
u, U	radial velocity [m/s] [–]
U_{CL}	contact line velocity [–]
v, V	axial velocity [m/s] [–]
$\boldsymbol{W}$	particle velocity [–]
We	Weber number [–]
z, Z	axial coordinate [m] [–]

Mathematical operators

D_τ	Lagrangian derivative towards τ
$d_{\tau,T}$	ordinary derivative towards τ or T
$\partial_{R,Z}$	partial derivative towards coordinates
$\overline{\nabla}$	nabla operator

Greek symbols

α	thermal diffusivity [m^2/s]
β	enhancement factor [–]
δ_{ij}	Kronecker symbol [–]
δ_m	monolayer thickness [m]
ε_{Slip}	slip coefficient [–]
ε_{YF}	wetting coefficient [–]
γ	surface tension [N/m]
η	dynamic viscosity [kg/(m s)]
κ_w^0	displacement frequency [1/s]
λ	displacement length [m]
ρ	density [kg/m^3]
$\bar{\sigma}$	shear stress component [–]
τ	dimensionless time [–]
θ	dynamic contact angle [rad, °]
θ_d	dynamic contact angle [rad, °]
θ_s	static contact angle [rad, °]

Subscripts

0	initial
1	droplet
2	substrate
abs	absolut
amb	ambient
g	gas phase
l	liquid phase
max	maximal
p	particle phase
s	surface
tot	total
v	vapor phase
z	axial direction
θ	azimuthal direction

capillary flows (solute Marangoni effect). Applying large heat fluxes from the substrate initiates the Leidenfrost-phenomenon, reducing the wettability tremendously. Fine particles dispersed on the surface of a liquid are moreover well known to reduce the liquid–solid wettability of the carrier liquid significantly (Aussillous and Quere, 2001), which is due to the increase in surface energy of the liquid–vapor interfacial tension with particle surface concentration. On the other hand, suspended particles might increase liquid–liquid wettability depending on the change in surface free energy after particle immersion (Goedel (2003)).

Despite this extensive work on the thermodynamic effects and thermal treatment of deposited nanoparticle suspension liquid, there does not exist up to the authors' knowledge a study detailing the inertia driven impact of micron-sized nanoink droplets. This is due to the generally weak tendency of nanosized particles to have a relative motion to the isothermal liquid matrix, justifying the treatment as a homogeneous fluid. Additional work on this topic appears to be rather unrewarding considering the amount of the literature published on the drop impact of simple liquids. However, although the volumetric particle loads in nanoinks are typically as low as 1.5–2 vol%, the particle content in terms of mass is considerably high, as much as 30–40 wt%, favoring inertia effects during impact. Nanoparticle suspension liquids exhibit a complex non-Newtonian rheology and the dynamics can be expected to be a strong function of the local particle arrangement inside the liquid.

The latter aspect shall be addressed within this work. The effect of ultrafine particles on the deposition process of micron-sized droplets (O(90 μm)), and particularly on

spreading is experimentally and numerically investigated herein and compared to the behavior of the corresponding pure liquid solvent of the suspension. The experiments are conducted with a high-speed camera and used to calibrate the numerical simulations obtained with a Galerkin FEM discretization of the unsteady, axis-symmetric Navier–Stokes equations in Lagrangian coordinates. The model employs two wetting models based on the uncompensated Young force at the contact line and tracks a representative number of computational particles, influenced by friction, diffusion and buoyancy forces. This allows making a statement of flow-driven particle structuring effects inside the liquid, a feature not readily accessible with experiments.

Toluene is, together with α-terpineol, the most commonly employed solvent for ultrafine gold particles of O(10 nm) for high concentrations in the novel field of technical nanoparticle ink utilization and used in this study as a reference (working) liquid. Copper and glass are employed as examples of substrate materials. Low impact velocities of O(1.5 m/s) ensure that no splashing occurs.

Section 2 details the experimental procedure; Sections 3 and 4 outline the fluid, respectively the particle model employed, including some details of the solution procedure. Section 5 discusses the results obtained and concluding remarks are made in Section 6.

2. Experimental setup

The micron-sized droplets were generated with a piezoelectrically driven drop-on-demand (DOD) jetting device (Attinger et al., 2000; Bieri et al., 2003; Haferl and Poulikakos, 2003), and allowing for the generation of monodispersed droplets with a diameter in the range of 60–100 μm. The visualization of the microdroplet impact with a time scale of the order of O(100 μs) has been reported earlier with strobe photography/videography (Yarin and Weiss, 1995), or more recently by splitting a time sequence to several frame grabbers as in Maier et al. (2000). In this work, a high-speed camera is used to visualize the droplet impact. The benefit lies in the possibility to track the impact of a single droplet whereas the strobe videography requires a continuous steady state droplet generation and a horizontal substrate translation after every impact of a droplet to provide a clean surface for the following droplet: since the surface is not always totally plane and homogeneous the reconstruction of the spreading process is difficult whereas with the high-speed camera the substrate stays immobile. To this end a triggered high-speed camera (Redlake MotionXtra™ HG-100K, USA) with up to 110 000 frames per second at 64×16 pixel resolution, was employed for the digital imaging. A microscope objective (Microtech Zoom 70, USA) was used to magnify the droplet images. An optical magnification of 29× on the CMOS sensor was utilized giving a spatial resolution of 3.6 μm in the object plane. The experimental setup is depicted in Fig. 1.
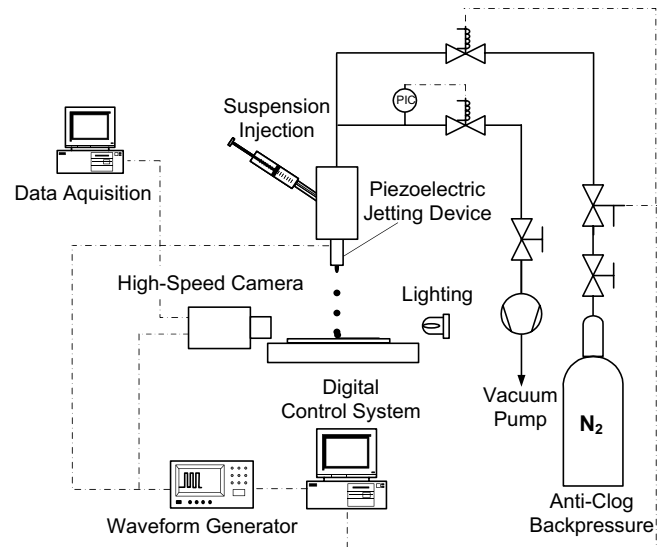

Fig. 1. Sketch of the experimental setup.

Three cases were considered, pure toluene on copper or glass and nanoink on copper. All results (spreading, contact angle) were obtained by visual inspection of each frame. Based on the limited resolution, the spreading values are accurate within ±5–8% tolerance and the values for the dynamic contact angle are accurate within 3–10° tolerance. The droplet diameter was $d_0 = 95 \pm 0.04$ μm and the droplet velocity right at the nozzle orifice was $v_n = 2 \pm 0.05$ m/s.

3. Fluid model

The mathematical description of the problem in a dimensionless Lagrangian form of the (isothermal) Navier–Stokes equations using the Artificial Compressibility Method (Chorin, 1997), reads

$$D_\tau P + \frac{\bar{\nabla} \cdot \boldsymbol{V}}{M^2} = 0 \quad \text{Continuity} \tag{1}$$

$$D_\tau \boldsymbol{V} - \bar{\nabla} \cdot \overline{\boldsymbol{T}} + \frac{\boldsymbol{n}_Z}{Fr} = 0 \quad \text{Momentum} \tag{2}$$

The dimensionless coordinates, velocities, time and pressure read

$$\text{(a) } R = \frac{r}{d_0} \quad \text{(b) } Z = \frac{z}{d_0} \quad \text{(c) } U = \frac{u}{v_0}$$

$$\text{(d) } V = \frac{v}{v_0} \quad \text{(e) } \tau = \frac{t}{d_0/v_0} \quad \text{(f) } P = \frac{p - p_{\text{amb}}}{\rho_l v_0^2} \tag{3}$$

with d_0 denoting the initial droplet diameter and v_0 the impact velocity. ρ_l is the liquid density and p_{amb} the ambient pressure. The dimensionless stress tensor and its components $\bar{\sigma}_{ij}$ are defined as follows:

$$\overline{\boldsymbol{T}} = \begin{bmatrix} \bar{\sigma}_{RR} & \bar{\sigma}_{RZ} & 0 \\ \bar{\sigma}_{RZ} & \bar{\sigma}_{ZZ} & 0 \\ 0 & 0 & \bar{\sigma}_{\theta\theta} \end{bmatrix}$$

$$\bar{\sigma}_{RR} = -P + \frac{2}{Re}\partial_R U,$$

$$\bar{\sigma}_{ZZ} = -P + \frac{2}{Re}\partial_Z V, \quad \bar{\sigma}_{\theta\theta} = -P + \frac{2}{Re}\frac{U}{R},$$

$$\bar{\sigma}_{RZ} = \frac{1}{Re}(\partial_Z U + \partial_R V) \tag{4}$$

The initial Reynolds, Froude, Mach and Weber number are defined as

(a) $Re = \dfrac{\rho_l v_0 d_0}{\eta_{\mathrm{ref}}}$ (b) $Fr = \dfrac{v_0^2}{d_0 g}$ (c) $M = \dfrac{v_0}{c_s}$

(d) $We = \dfrac{\rho d_0 v_0^2}{\gamma}$ (5)

η_{ref} is a dynamic reference viscosity of the pure liquid, g is the gravitational acceleration, c_s the artificial speed of sound and γ a reference surface tension of the pure liquid. At the initial stage, the droplet is spherical and moves downwards with a dimensionless velocity of -1. In this stage, the pressure-field is uniform ($P_0 = 4/We$). The velocities of the splat nodes in contact with the substrate are set to zero except the nodes in vicinity of the contact line, where only the no-penetration condition is set. The usual axis-symmetric condition is applied to all splat parameters on the Z-axis.

Eqs. (1) and (2) are spatially discretized with a Galerkin FEM description. The weak formulation of the momentum equations reads

$$\int_\Omega \phi_k D_\tau \boldsymbol{V} + \vec{\nabla}\phi_k \cdot \overline{\boldsymbol{T}} + \phi_k \cdot \begin{pmatrix} \bar{\sigma}_{\theta\theta}/R \\ 1/Fr \end{pmatrix} \mathrm{d}\Omega = \int_{\partial\Omega} \phi_k (\overline{\boldsymbol{T}}^{\mathrm{s}})^T \cdot \boldsymbol{n}^{\mathrm{s}} \mathrm{d}\Gamma \tag{6}$$

The upper script 's' denotes the evaluation at the surface. For elements at the free surface, the projection of the stress tensor $\overline{\boldsymbol{T}}$ onto the outer surface normal in (6) can be rewritten with Laplace's equation (Landau and Lifshitz, 1959):

$$(\overline{\boldsymbol{T}}^{\mathrm{s}})^T \cdot \boldsymbol{n}^{\mathrm{s}} = -2\frac{\overline{H}}{We}\boldsymbol{n}^{\mathrm{s}} \tag{7}$$

$\overline{H} = H d_0$ is the dimensionless mean curvature defined with

$$2\overline{H} = \frac{1}{R}\frac{Z'}{[(R')^2 + (Z')^2]^{1/2}} + \frac{(R'Z'' - Z'R'')}{[(R')^2 + (Z')^2]^{3/2}}$$

$$= \frac{1}{R}t_Z + \|\vec{t}\|' \tag{8}$$

$(.)' \equiv d_s(.)$ denotes derivation to the arc length s. The integration of Eq. (8) over the element boundary uses a second-order shape function of the free surface line elements and in addition integration by parts for the second curvature term to avoid the derivation of the tangential vector. Details can be found in Waldvogel (1995).

Spontaneous wetting or de-wetting occurs when the Gibbs free energy of the system can be reduced. A conventional hydrodynamic model requires the allowance of slip

at the contact line to avoid singularities in mass and momentum conservation and an additional wetting model to capture the dynamics at the contact line (Dussan and Davis, 1974). Herein it is assumed that the uncompensated Young force occurring for contact angles differing from the static one is compensated by fluid stresses in a small, but finite contact line segment (CL-Seg.) (Dietzel and Poulikakos, 2003):

$$\left[(\overline{\boldsymbol{T}}^{\mathrm{s}})^T \cdot \boldsymbol{n}^{\mathrm{s}} \cdot \boldsymbol{e}_R\right]_{\mathrm{CL\text{-}Seg.}} = \frac{\varepsilon_{\mathrm{YF}}}{We}[\cos(\theta_{\mathrm{s}}) - \cos(\theta_{\mathrm{d}})] \tag{9}$$

$\boldsymbol{e}_R$ is the radial unity vector, θ_{s} is the static and θ_{d} is the dynamic contact angle, respectively. $\varepsilon_{\mathrm{YF}}$ is an empirical constant of O(1). Note, that for static conditions (no fluid shear stress) with $\theta_{\mathrm{d}} = \theta_{\mathrm{s}}$, the Young–Dupré-equation is fulfilled:

$$\frac{\cos(\theta_{\mathrm{s}})}{We} = \frac{1}{We_{\mathrm{s0}}} - \frac{1}{We_{\mathrm{sl}}} \tag{10}$$

The Weber-number for the solid–gas (index s0) and the solid–liquid (index sl) interface is defined as in Eq. (5)d), with the liquid–vapor interfacial tension replaced by the corresponding values for the solid–gas and the solid–liquid interface, respectively. The values for the static contact angle θ_{s} were approximated directly from the experiments. The dynamic contact angle is provided by the simulation due to the Lagrangian formulation. When dynamic slip friction at the contact line is not negligible, it can be modeled through the conventional Navier-slip model. With this, relation (9) reads

$$\left[(\overline{\boldsymbol{T}}^{\mathrm{s}})^T \cdot \boldsymbol{n}^{\mathrm{s}} \cdot \boldsymbol{e}_R\right]_{\mathrm{CL\text{-}Seg.}} = \frac{\varepsilon_{\mathrm{YF}}}{We}[\cos(\theta_{\mathrm{s}}) - \cos(\theta_{\mathrm{d}})] - \frac{\varepsilon_{\mathrm{slip}}}{Re}U_{\mathrm{CL}} \tag{11}$$

$\varepsilon_{\mathrm{Slip}}$ is a slip coefficient of O(10^2) and U_{CL} is the current contact line velocity which is solved in conjunction with the other fluid velocities.

Eq. (11) is compared to a molecular kinetic model of dynamic wetting originally suggested by Blake and Haynes (1969) for liquid–liquid displacement which understands wetting as an adsorption/desorption process of liquid molecules by the substrate. The dimensionless contact line velocity is derived as

$$U_{\mathrm{CL,Blake}} = \frac{2\kappa_w^0 \lambda}{v_0}\sinh\left\{\frac{\rho v_0^2 d_0}{2nk_{\mathrm{B}}T}\frac{[\cos(\theta_{\mathrm{s}}) - \cos(\theta_{\mathrm{d}})]}{We}\right\} \tag{12}$$

κ_w^0 is the molecular equilibrium displacement frequency of O($10^{11}1/s$) and λ is the molecular displacement length, which can be approximated for copper to be 2.1 Å. The number of adsorption sites n per unit area is for homogeneous surfaces just the squared reciprocal of the displacement length ($n = \lambda^{-2}$). k_{B} and T are the Boltzmann constant and the absolute temperature, respectively. Note that the contact line velocity in (12) is explicitly known since the static contact angle is provided by the experiments and the dynamic contact angle is derived from the simulation. $U_{\mathrm{CL,Blake}}$ is therefore not solved through the

FEM-matrix system but used as a boundary condition, contrary to U_{CL} defined in (11).

4. Particle model

The volumetric particle content of the suspension liquids considered in this study is rather low (about 1.5 vol%). The volume of the suspended particles is therefore neglected for the simulation of the liquid, justifying the assumption of a one-phase-fluid model described above. The trajectory of small particles with a low particle Reynolds number, disregarding particle–particle and particle–wall interaction, can be described with the particle motion equation derived by Maxey and Riley (1983). In case of a large particle-to-liquid density ratio, Elghobashi and Truesdell (1992) pointed out that the pressure gradient term, added mass term and to some extent also the Basset history term are small compared to Stokes' drag and buoyancy. Ultrafine particles of $O(10\,nm)$ are at the lower size limit where classical Stokesian dynamics applies (Brady, 2001). Thermophoresis (in a non-isothermal case) and diffusion forces become increasingly important for these kind of particles (Hinds, 1998), especially when the advective propulsion vanishes. The dimensionless Newton's second law for the particles in this study (without thermophoresis) reads therefore:

$$d_\tau \boldsymbol{W} = -\frac{18}{Re}\left(\frac{d_0}{d_p}\right)^2 \frac{\rho_l}{\rho_p}(\boldsymbol{W}-\boldsymbol{V}) - \frac{6k_B T}{\pi d_p^3 \rho_p v_0^2}\frac{\bar{\nabla}c}{c}$$
$$+ \left(1 - \frac{\rho_l}{\rho_p}\right)\frac{1}{Fr}\frac{\boldsymbol{g}}{g} \qquad (13)$$

where $\boldsymbol{W}$ is the dimensionless particle velocity, d_p is the particle diameter, ρ_p is the particle density and c is the volumetric particle concentration. The left-hand-side term of Eq. (13) considers the particle inertia which is by definition of $O(1)$. The first term on the right is the Stokes' friction between the particle and the surrounding liquid, the second captures the particle diffusion force and the last models the (weak) buoyancy force. The particle Stokes number Stk_p defined as the ratio between the particle relaxation time $t_{p,char}$ and the characteristic flow time $t_{l,char}$, Eq. (14), is of $O(10^{-6})$ in the applications presented here, which implies that the particles should follow the flow instantaneously:

$$Stk_p = \frac{t_{p,char}}{t_{l,char}} = \frac{\rho_p d_p^2}{18\eta}\frac{v_0}{d_0} = \frac{\rho_p}{\rho_l}\left(\frac{d_p}{d_0}\right)^2 \frac{Re}{18} \qquad (14)$$

Relation (13) is transferred for every time step into a simple first-order inhomogeneous ordinary differential equation (ODE) by assuming that everything except the particle velocity is constant. This ODE is solved analytically for every time step, providing the current particle velocity. This solution method was successfully cross-checked with an implicit Euler integration scheme.

Despite the fact that the particle volume is negligibly small, the particles contribute about 30 wt% in overall droplet mass. The inertia of the particles is coupled back to the liquid through assigning to those nodes a higher inertia which are direct neighbors of particles. The following procedure is used to limit the number of computational particles: first, the initial droplet cross-sectional area is divided in equally sized sub-areas, whereby one computational particle is placed in the center of each sub-area. The size of these sub-areas is user-defined and determines the number of computational particles. These computational particles are then weighted with a factor w_p, Eq. (15), according to the volume the rotated sub-area element corresponds to:

$$w_p = 12c_0 R_{av}^{(e)} A_{sub}^{(e)}\left(\frac{d_0}{d_p}\right)^3 \qquad (15)$$

where $R_{av}^{(e)}$ is the average distance of the element from the axis of rotation (Z-axis), $A_{sub}^{(e)}$ is the cross-section of the sub-element and c_0 is the initial volumetric particle concentration. Particles placed in elements further away from the axis of symmetry have therefore a larger weighting factor than particles placed in elements closer to the centerline since these computational particles represent a larger number of real particles. The initially assigned weighting factor is kept constant for each particle throughout the simulation (no coagulation).

The change of viscosity with particle concentration is considered using the empirical Krieger–Dougherty relation described in Krieger and Dougherty (1959). With the experimentally found exponent of −2 it reads (Quemada, 1977):

$$\frac{\eta(c)}{\eta_{ref}} = \left(1 - \frac{c_{eff}}{c_{max}}\right)^{-2} \qquad (16)$$

η_{ref} is herein the liquid viscosity at zero particle concentration and c_{max} is the particle concentration when the liquid-particle suspension starts to behave as a solid. In Eq. (16), the core particle concentration c was replaced by an effective particle concentration of $c_{eff} = 1.875c$ to capture the influence of the monolayer surrounding the sterically stabilized particles. This corresponds to a monolayer thickness of $\delta_m = 0.12d_p$ (Mewis and Vermant, 2000). The parameter c_{max} was set to 0.15, in agreement with values given in the literature for a TiO$_2$-nanoparticle suspension liquid (Tseng and Lin, 2003). With this the average reduced viscosity is 1.515. No viscosity dependence on the shear rate is assumed in this study since no reliable experimental data were available. Note that the implementation of a variable viscosity does not introduce an additional source term in the discrete FEM momentum equation due to the usage of Gauss' theorem and is performed by the evaluation of a local element Re-number, based on Eq. (5a).

The solution procedure for the flow was outlined in Dietzel et al. (2003). The previously used commercial meshing tool Hypermesh$^{®}$ was replaced by the public-domain
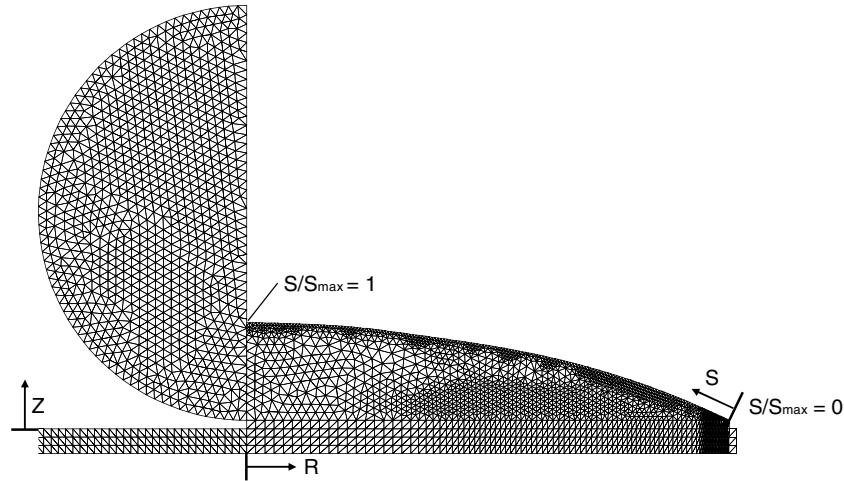
Fig. 2. Example grids for initial (left) and final (right) droplet shape.

software Mesh2D. The routines were modified to have an additional mesh refinement in the contact area to resolve small changes in spreading and at the free surface to minimize the mass error during remeshing. The left side of Fig. 2 depictures an initial mesh, whereas the right side shows a typical mesh at very late stages of the droplet impact simulation (dimensionless time 5).

Typical computations employed about 3500 elements on average. The simulations were performed either on a Pentium III PC (1 GHz), DEC workstation or a Pentium IV PC (3 GHz). Simulations without particles took at least 84 h on the fastest machine (PIV) to complete 80 000 time steps. Simulations containing particles (represented by about 7500 computational particles) took at least 140 h for the same number of steps. The simulation code was extensively tested to ensure mass and energy conservation. For the mesh density and time step utilized, both mass and energy were conserved within a final error of less than 1% compared to the initial values. Furthermore, it was verified that mesh and time step independent solutions were obtained. Since the integration of the particle path is done in a semi-analytical fashion, particle accuracy is only limited by the local accuracy of the fluid velocity and by the linear interpolation to locate the particle inside an element.

All simulations used an initial droplet diameter of $d_0 = 95 \, \mu\text{m}$ and an impact velocity of $v_0 = 1.5$ m/s which provides with the fluidic properties of pure toluene at 25 °C (density $\rho_{\text{ref}} = 867 \, \text{kg/m}^3$, viscosity $\eta_{\text{ref}} = 0.56 \times 10^{-3}$ Pa s, surface tension $\gamma = 27.93 \times 10^{-3}$ N/m) an initial *Re*-number of 220 and an initial *We*-number of 6.64. The nozzle exit velocity ($v_{\text{n}} = 2.0$ m/s), measured approximately 1 mm above the substrate in the experiments, differs from the impact velocity used to initialize the simulations. It was not possible to directly obtain the latter from the experiments. To reason the difference, consider Newton's second law for the spherical drop in a free fall between the nozzle and the substrate. The viscous (Stokes') friction force dominates over the form drag for small bodies, therefore:

$$md_t v = F_{\text{grav}} - F_{\text{fric}} = mg - 3\pi\eta_{\text{g}}d_0 v \quad m = \rho_{\text{ref}}\frac{\pi}{6}d_0^3 \quad (17)$$

Herein is the gas density $\rho_{\text{g}} = 1.2 \, \text{kg/m}^3$ and the gas viscosity $\eta_{\text{g}} = 1.8$ Pa s. Solving this differential equation for a start velocity of $v_{\text{n}} = 2.0$ m/s leads to an impact velocity of $v_0 = 1.96$ m/s. However, the classical Stokes' friction force is only valid if the body is moving in an infinite medium and it is known that the friction is by orders of magnitudes larger in the direct proximity of a wall aligned vertically to the in-flight direction: Brenner (1961) derived that the friction force acting on a spherical particle approaching a rigid wall is between $1.13 \leqslant \beta \leqslant 9.25$ larger than captured by the Stokes' friction if the distance x of the particle to the wall is between $10.1 \geqslant 2x/d_0 \geqslant 1.13$ and asymptotically approaches infinity for even smaller distances. Here the droplet moves in the range of $21.0 \geqslant 2x/d_0 \geqslant 0$ and using an average friction enlargement factor of $\beta = 12$ in Eq. (17) leads to the impact velocity of $v_0 = 1.5$ m/s which gave the best results in the simulation.

The same (three) liquid–substrate configurations were considered in the simulation as in the experiments and the corresponding static contact angles ($\theta_{\text{s}} = 25°$ for pure toluene on copper, $\theta_{\text{s}} = 29°$ for pure toluene on glass, $\theta_{\text{s}} = 24°$ for nanoink on copper) needed for Eq. (9) were adopted from the latter. The initial particle content for the nanoink-case was 1.5 vol%.

5. Results and discussion

Fig. 3 shows the spreading radius R_{CL} versus time τ captured from the experiments with the high-speed camera (index 1). Case (a) is pure toluene on copper, case (b) is pure toluene on glass and case (c) is toluene with particles on copper. All spreading values shown are accurate within ± 5–8% tolerance. The most pronounced feature is the reduced spreading for the case involving particles for long times. At dimensionless time $\tau = 8.0$ ($t = 0.51$ ms), spreading is reduced about 30% by the presence of particles for
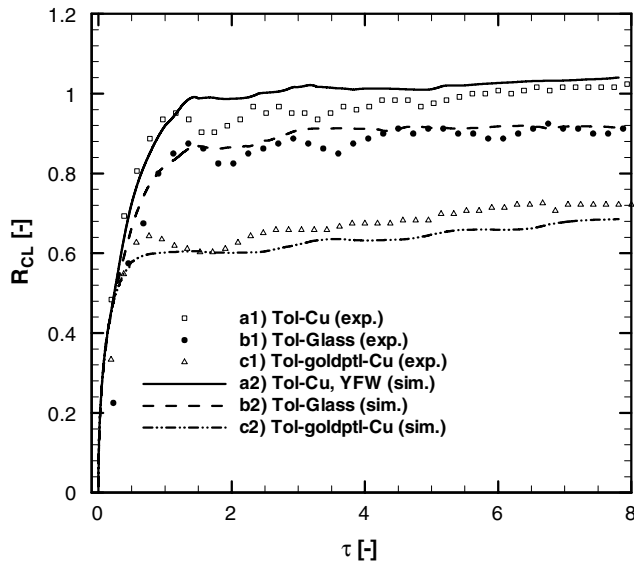
Fig. 3. Spreading radius R_{CL} versus time τ: (a) toluene on copper w/o particles; (b) toluene on glass w/o particles; (c) toluene on copper w/ particles. Index 1: experiment; index 2: simulation.

the toluene–copper-system. This result resembles earlier findings that particle content reduces the liquid–solid wettability due to the enhancement of the liquid–vapor interfacial tension (Aussillous and Quere, 2001). Although the added particle mass emphasizes inertial effects potentially increasing spreading, these additional inertial forces are overcompensated by viscous and contact line pinning forces as well as by the reduced wettability, hindering spreading as apparent from the experiment.

Spreading of pure toluene on glass is about 10% less than on copper for the same time instant, as lines (a) and (b) indicate. The difference is however less pronounced than it could be expected by just considering the about 20 times larger surface energy of pure copper (spreading parameter $\widetilde{S} = \gamma_{s0} - \gamma_{sl} - \gamma_{sv} > 0$, De Gennes, 1985) compared to glass, which might be even increased by oxidation of the copper surface. Generally, all cases show the typical two-stage spreading evolution in time (De Gennes, 1985): spreading is rapid during the initial stages ($d_\tau R_{CL} \propto 1.26$) and very slow during later stages ($d_\tau R_{CL} \propto 8.6 \times 10^{-3}$) driven by the uncompensated Young force. Cases (a) and (b) show an intermediate rest in spreading and a short de-wetting phase at about $\tau = 1.2$. Intermediate rest in spreading for case (c) occurs earlier, at about $\tau = 0.8$ with a less pronounced de-wetting zone. The spreading radius value in the secondary spreading regime oscillates for the cases without particles, whereas the nanoink shows a staged spreading with noticeable rests. However, the mean long-time spreading rates are almost identical for all cases and independent of particle content. This leads to the conclusion that particles influence primarily the initial spreading, causing a constant off-set in spreading between cases with and without particles for long times. The different behavior during the initial spreading state can be explained with a higher apparent viscosity of the toluene containing particles. As outlined in Section 3, sterically stabilized dispersions exhibit a non-Newtonian, shear-thinning (low shear) or shear-thickening (high shear rate) viscosity. The result obtained within this study suggests a thickening effect due to the high shear during the inertia-dominated primary spreading regime, leading to a lower apparent *Re*-number.

Simulations (index 2 in Fig. 3) resemble the experimental results for the following empirical contact line parameter pairs [ε_{YF}, ε_{Slip}], see Eq. (11): Case (a) [0.75, 1×10^2], case (b) [0.45, 1×10^2] and case (c) [0.15, 0.33×10^3]. The interest in these parameter findings is threefold. First they provide a measure of the interaction strength between the liquid and the solid starting from an intense interaction (leading to a pronounced wetting) in case of pure toluene on copper, reduced interaction for the toluene–glass system and finally a deteriorated interaction in case of the nanoink on copper. Second, the contact line friction increases by almost an order of magnitude if particles are present. This can be justified with the lock-in of the nanosized particles in surface inhomogeneities of the substrate leading to temporary contact line pinning. Last and as a summary, the mere out-of-balance Young force is not sufficient to capture the wetting dynamics: the parameters ε_{YF} and ε_{Slip} are not freely interchangeable, meaning that an increased ε_{YF} (increased wetting force) and an increased ε_{Slip} (increased contact line friction) will not result in the same spreading dynamics. This is due to the dual effect of increasing ε_{Slip}: this measure will increase the contact line friction but also in turn the dynamic contact angle, leading to a larger uncompensated Young force and a pronounced stick-slip motion of the contact line as observed in the nanoink spreading.

The short de-wetting stage as seen in the experiments is not well captured in the model although the initiating recoiling motion of the droplet center builds up also in the simulations, reducing the contact angle at some point below the static value. However, the contact line friction is usually larger for the wetting of an initially dry substrate than for de-wetting. Therefore, a smaller ε_{Slip} is needed for the de-wetting stage which was not incorporated in the present model. Note in this respect that the experimentally observed de-wetting stage is less emphasized for the nanoink spreading, although the recoiling motion is intensified due to the reduced radial droplet extent. This supports the view of increased contact line friction for the case involving particles.

Fig. 4a shows the spreading radius versus time as a comparison between simulations using either Eq. (11) or the adsorption/desorption model (AWM, Eq. (12)) at the contact line, each for pure toluene and a copper substrate. The dimensionless adsorption frequency in (12),

$$\bar{\omega}_{CL}^0 = \frac{2\kappa_w^0 \lambda}{v_0} \tag{18}$$

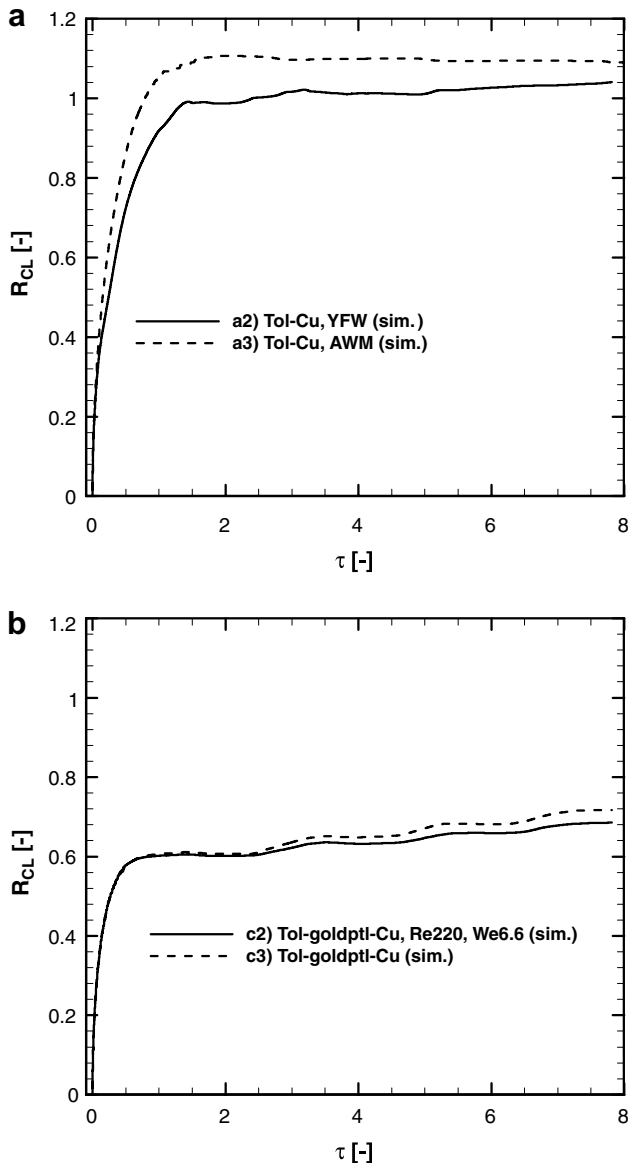was approximated to equal 15.0. The AWM overpredicts spreading during the initial spreading regime which is

Fig. 4. (a) Comparison of spreading radius R_{CL} versus time τ for two different wetting models (a2 – Young force wetting model, Eq. (11), a3 – adsorption wetting model, Eq. (12)); (b) Comparison of spreading radius R_{CL} versus time τ for suspension involving discrete particles (c2) and fictitious homogeneous liquid of similar total density and viscosity (c3).

explained with the absence of line friction modeling in relation (12). Another limitation of the adsorption wetting model is the constant spreading value in the Young-force spreading regime, a consequence of the fixed relationship between contact line velocity and contact angle. However, (12) simplifies the numerical treatment of the contact line and the respective simulations are numerically more stable than those using relation (11), in expense of only a slight decrease in accuracy.

Fig. 4b compares the spreading radius versus time for the discrete particle model employed in this study with a simulation using a fictitious homogeneous liquid of increased density (1143 kg/m instead of 867 kg/m,

corresponds to 1.5 vol% particle content), an increased viscosity (8.9×10^{-4} Pa s instead of 5.6×10^{-4} Pa s) and an increased surface tension compared to pure toluene to capture the influence of the gold particles on inertia, dissipation and cohesion. Both cases are identical during the inertia-dominated spreading regime, demonstrating that the inertia coupling between the discrete computational particles and the discrete nodes representing the liquid phase is successful. The cases differ only slightly during the Young-force dominated spreading regime.

Fig. 5a–c provides a comparison of the apparent dynamic contact angle (θ_d) evolution in time between experiments (index 1) and simulations (index 2) for the three cases (a: pure toluene on copper, b: pure toluene on glass, c: nanoink on copper). The experimental values are certain within $\pm 10°$ for very early stages and $\pm 3–4°$ for later stages of the impact process but are nevertheless useful to discuss some general aspects of the process. It can be seen that the qualitative evolution is similar for all cases consisting of a sharp decrease in contact angle during the inertia-dominated spreading regime and a relatively slow approach of the static conditions for long times. However, the toluene on copper case invoking particles (Fig. 5c shows a significantly prolonged time to reach the equilibrium state, although static contact angles at long times are for all cases identical within a range of 5°. Additionally, this case features slight oscillations in the contact angle value within dimensionless time 2.0–6.0 without pronounced changes in spreading. This suggests a weak contact line pinning due to particle interaction and lock-in with the copper substrate.

Simulations recover the experimental findings within the measurement uncertainty for cases (a) and (b). For case (c) involving particles, the simulated contact angle evolution is shifted ($\Delta\tau_{shift} \approx 0.5$) during the initial spreading regime compared to the cases without particles. Although this meets the general trend of a delayed contact angle evolution seen from the experiments, the simulation overpredicts its extent especially in the time range $\tau = 0.0–1.0$. At later times, the oscillation of the dynamic contact angle and the tendency of a prolonged time to reach equilibrium are generally captured but consistently overpredicted. The oscillations are weaker and damped out quicker in the experiments than predicted by the model. Numerical tests with an increased surface tension, approximated by the following formula originally suggested for liquid metal (Egry, 1993),

$$\gamma_{ptl} = \frac{\eta_{ptl}}{\eta_0}\gamma_0 \qquad (19)$$

led as expected to an increase in oscillation frequency but did not reduce the amplitude. Moreover this measure increases the wetting force, as apparent in Eq. (9), leading to an enhanced spreading. The fluctuation in the contact angle right at the beginning of the droplet impact is a numerical artifact caused by the specific attachment
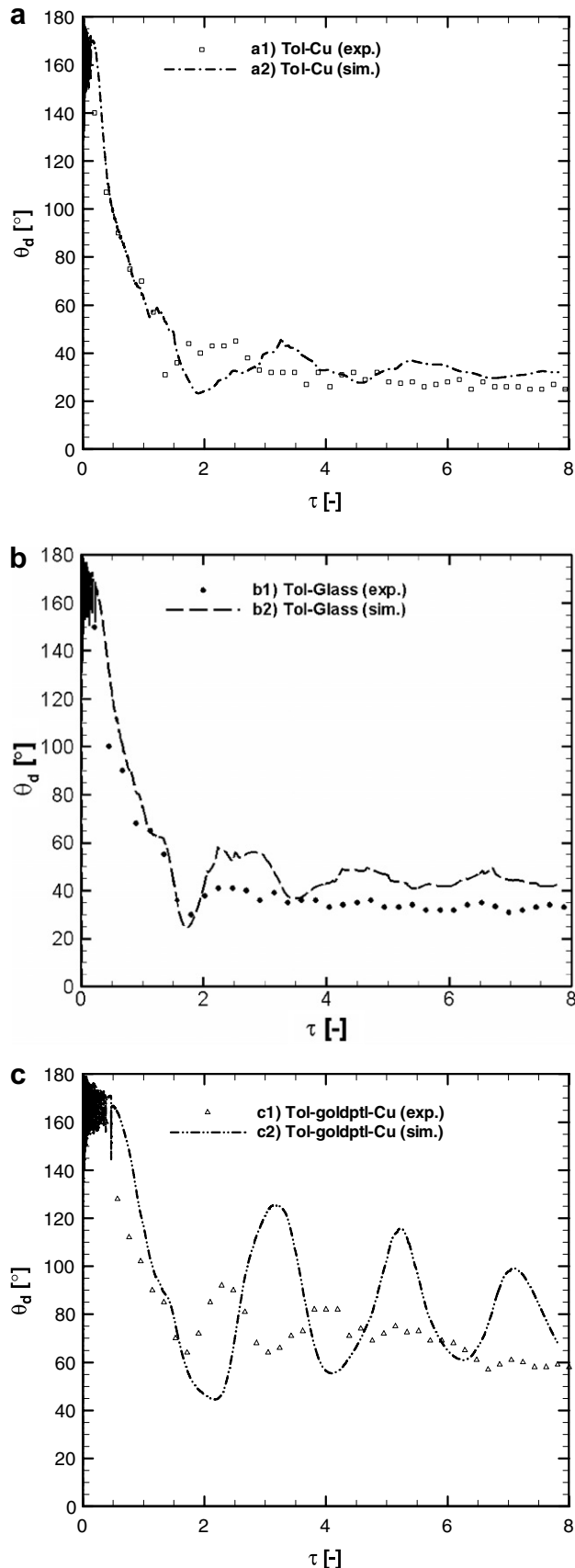
Fig. 5. Apparent dynamic contact angle θ_d versus time τ: (a) toluene on copper w/o particles; (b) toluene on glass w/o particles; and (c) toluene on copper w/ particles. Index 1: experiment; index 2: simulation.
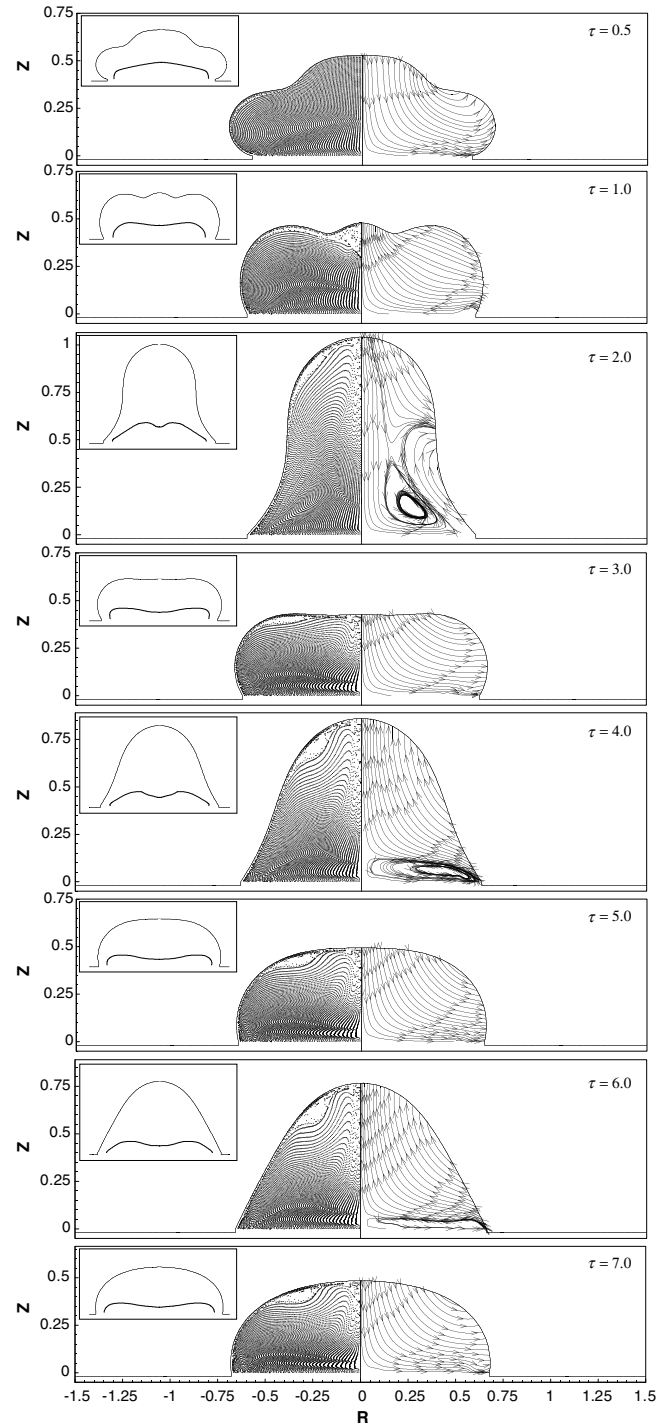

Fig. 6. Simulated particle position and streamlines for toluene on copper, w/ particles, times $\tau = 0.5$, 1, 2, 3, 4, 5, 6, 7 (from top to bottom). Insets: Separation line between outer and inner particle region.

algorithm of fluid elements to the substrate as discussed in Haferl and Poulikakos (2002).

Fig. 6 shows the different stages of droplet spreading for the dimensionless times $\tau = 0.5$, 1, 2, 3, 4, 5, 6 and 7 in case of a toluene droplet deposited on a copper substrate containing particles. The left sides of the depicted droplets render the position of the computational particles, exaggerating however the size of the particles for the sake

of readability. The right sides illustrate the streamlines. It can be seen that the reduced spreading compared to the pure toluene case (not shown for brevity) leads to a generally more compact droplet, favoring a significantly enhanced oscillatory recoiling motion. Although the small particle Stokes number defined in Eq. (14) suggests that the particles should follow the outer flow conditions instantaneously, Fig. 6 reveals that the particle motion in the upper center region is delayed during the first recoiling stage (see $\tau = 1.0$). The Stokes number defined in relation (14) was obtained from (13) using the initial droplet diameter divided by the impact velocity as the characteristic time scale ($t_{\text{l,char.}} = d_0/v_0$) and the initial impact velocity as characteristic velocity of the flow. These global time and velocity scales (and therefore the Stokes number) are not representative for the recoiling phase which is driven through the restoring surface tension force. This causes the inertia term in Eq. (13) to be significantly larger than unity. If $t_{\text{rc,char.}}$ is the characteristic time scale and $v_{\text{rc,char.}}$ the characteristic velocity scale of the flow during recoiling, then

$$\frac{t_{\text{rc,char.}}}{t_{\text{l,char.}}} \frac{v_0}{v_{\text{rc,char.}}} d_\tau \boldsymbol{W} = \mathrm{O}(1) \tag{20}$$

and a modified Stokes number can be introduced defined as

$$Stk_{\text{p}}^* = \frac{t_{\text{l,char.}}}{t_{\text{rc,char.}}} \frac{v_{\text{rc,char.}}}{v_0} Stk_{\text{p}} \tag{21}$$

Fig. 7 plots the axial derivative of the absolute axial velocity on the droplet center versus axial coordinate briefly after impact ($\tau = 0.0$, solid line) and for the strongest recoiling motion ($\tau = 0.93$, dash-dotted line). From this figure one can derive
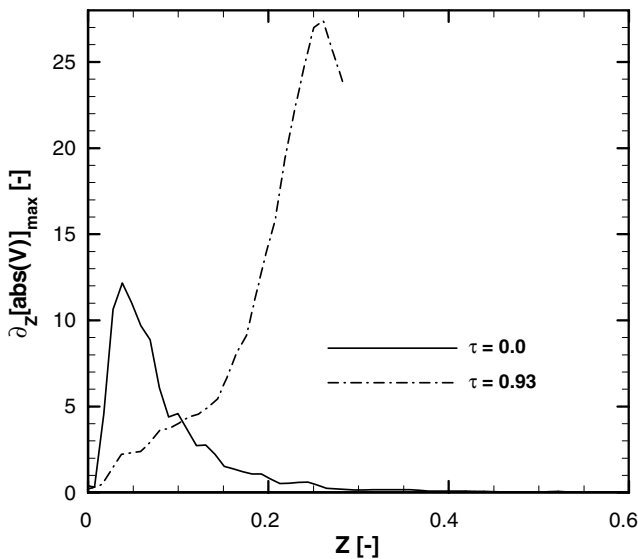

Fig. 7. Axial gradient of absolute axial velocity on droplet center briefly after droplet impact (solid) and during recoiling (dashed line).
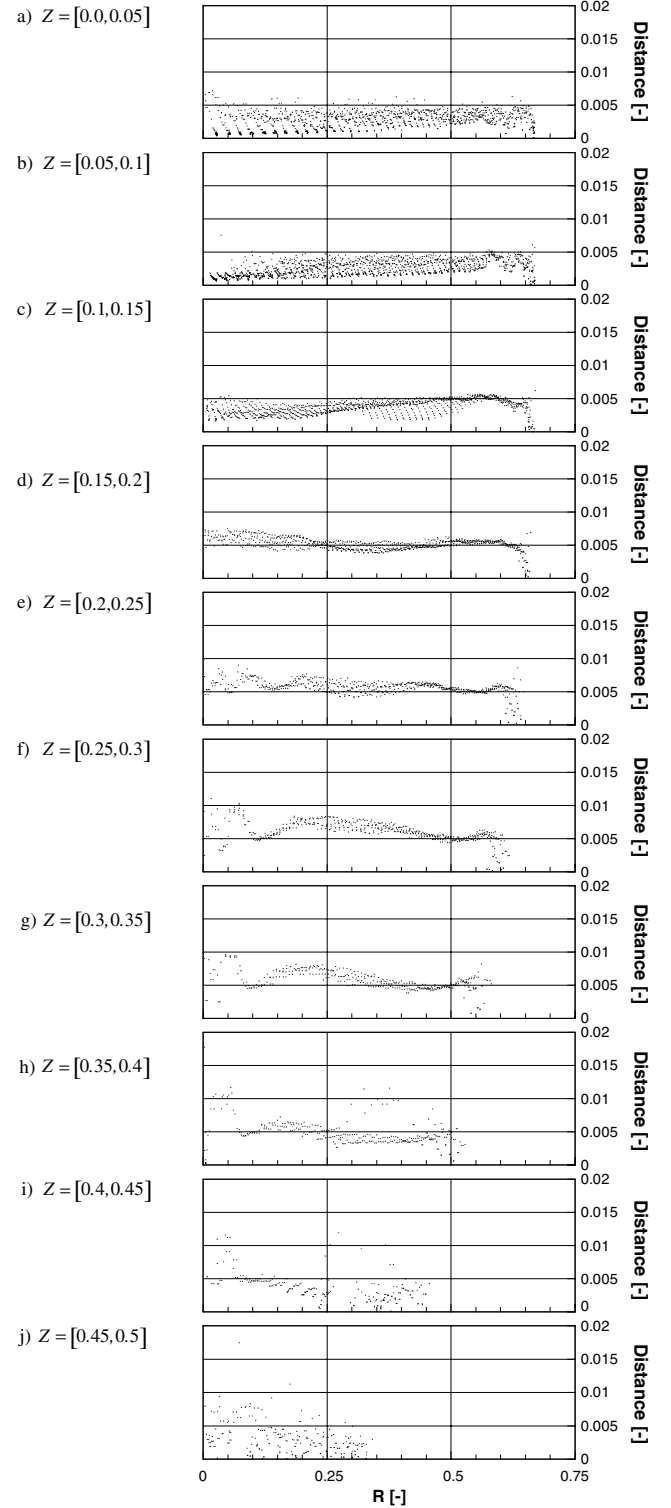

Fig. 8. Minimum interparticle distance at time $\tau = 7.0$. Shown are slices in radial direction of $\Delta Z = 0.05$ width starting from $Z = 0.0$ to $Z = 0.5$.

$$\partial_Z[\text{abs}(V)]_{\text{max}} = \frac{\partial_z[\text{abs}(v)]_{\text{max}}}{1/t_{\text{l,char.}}} = \frac{t_{\text{l,char.}}}{t_{\text{char.,min}}} \approx 25$$

$$\approx \frac{t_{\text{l,char.}}}{t_{\text{rc,char.}}} \tag{22}$$
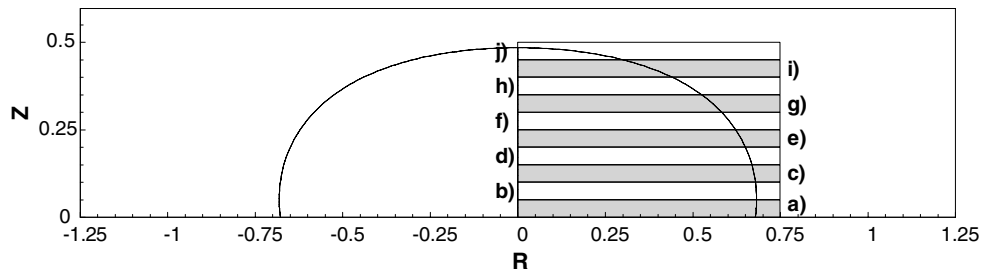
Fig. 9. Illustrations of particles zones shown in Figs. 8 and 10.

z and v are herein the axial coordinate and the axial velocity with dimensions. Furthermore, axial peak velocities during recoiling (not shown here for brevity) can be about 2.5 times larger than the initial impact velocity. With this, Stk_p^* is of $O(10^{-3})$, allowing a small inertia-driven particle slip velocity during recoiling. It has to be added that this effect is even underpredicted in the model since slip corrections of Stokes' correlation valid for very small particles is not incorporated.

The diluted particle distribution in the upper droplet region is only partly compensated by the particle diffusion force during the rest of the impact process. On the contrary, particles are accumulated in proximity of the substrate in the bulk liquid. Two particle regions can be defined: an outer flow region (region 1) with strong particle motion, effectively re-dispersing the particles, and an inner region (region 2), in which particle motion is significantly reduced. This region approximately coincides with the recirculation zone (caused by the wall friction) during recoiling. The separation line between those two regions is drawn for each instant in the insets of each picture in Fig. 7. It is deduced that the oscillatory flow motion initiates a structuring of those particles located in the inner region. This particle structuring needs to be stressed since it potentially provides an additional mechanism to explain the characteristic cross-sectional shape as encountered during the printing and drying of particle suspension droplets (Fuller et al., 2002). This shape is often referred to as bowl or trough shape with an elevated surface at the outer regions with a dimple in the center. Previous studies attributed this effect solely to the occurrence of Marangoni convection due to localized heating through e.g. laser irradiation (Bieri et al., 2003; Chung et al., 2004). However, the accumulation of particles in the droplet circumference can also be observed during pure drying without additional heat source where thermocapillarity-induced flows are negligible. The established explanation of the latter phenomenon focuses on the increased evaporation rate at the contact line (caused through a depression of the vapor concentration in the ambient gas at the contact line), leading to a flow of suspension liquid from the interior outwards and simultaneously accumulating particles at the contact line (ring stain formation) (Deegan et al., 1997). This mechanism is restricted to a limited mass accumulation since it becomes increasingly difficult for the solvent to advect to

the contact line with rising mass deposition. However, Maenosono et al. (1999) mention the possibility that the capillary pressure between the agglomerated particles supports the solvent transport. All of these studies implicitly assume segregation between particles and carrier liquid only due to evaporation. The current study proposes that the flow patterns during recoiling lead to a segregation of particles from the solvent and a pre-structuring in the region 2 defined above, creating a dimple in the cross-sectional particle distribution.

Fig. 8 shows the minimum interparticle distance for each computational particle as a function of radial particle location for the dimensionless time $\tau = 7.0$. The droplet height is herein cut in equally spaced slices of width $\Delta Z = 0.05$, starting from $Z = [0.0, 0.05]$ for the top figure and ending at $Z = [0.45, 0.5]$ for the last figure, as illustrated in Fig. 9. Although the absolute value for the interparticle distance is a function of the number of computational particles initially seeded, the qualitative trend is general, since no particle interaction is assumed. Apparently, the smallest interparticle distance exists at the interfaces, i.e. at the liquid–substrate interface (first slice) and at the free surface (all slices for maximum radial location). The latter particle agglomeration illustrates the tendency of colloidal liquids for crust formation at the free surface. The bandwidth of interparticle distance (i.e. the range of smallest interparticle distances occurring) has a minimum at $Z = [0.15, 0.2]$ (fourth slice), whereas it is maximum for the droplet top region (last three slices). This bandwidth can be considered as an indication of particle structuring: a large bandwidth suggests low particle order and a low bandwidth implies a high degree of particle structuring. Considering slice 4 (minimum bandwidth), the highest particle order appears at radial locations between $R = 0.5$ and $R = 0.6$.

Fig. 10 depicts the number of neighbors of each particle within a certain cutoff-distance for the same instant and slices as in Fig. 8. The absolute value is again a function of the number of computational particles used and additionally of the specific cutoff-radius-value chosen. However, as for the minimum interparticle distance, qualitative results are general. The number of neighbors reduces significantly at interfaces, which is physical for the free surface and the liquid–substrate interface but an artifact of the method for the droplet center, i.e. $R = 0$. This artifact occurs since only one half of the droplet and
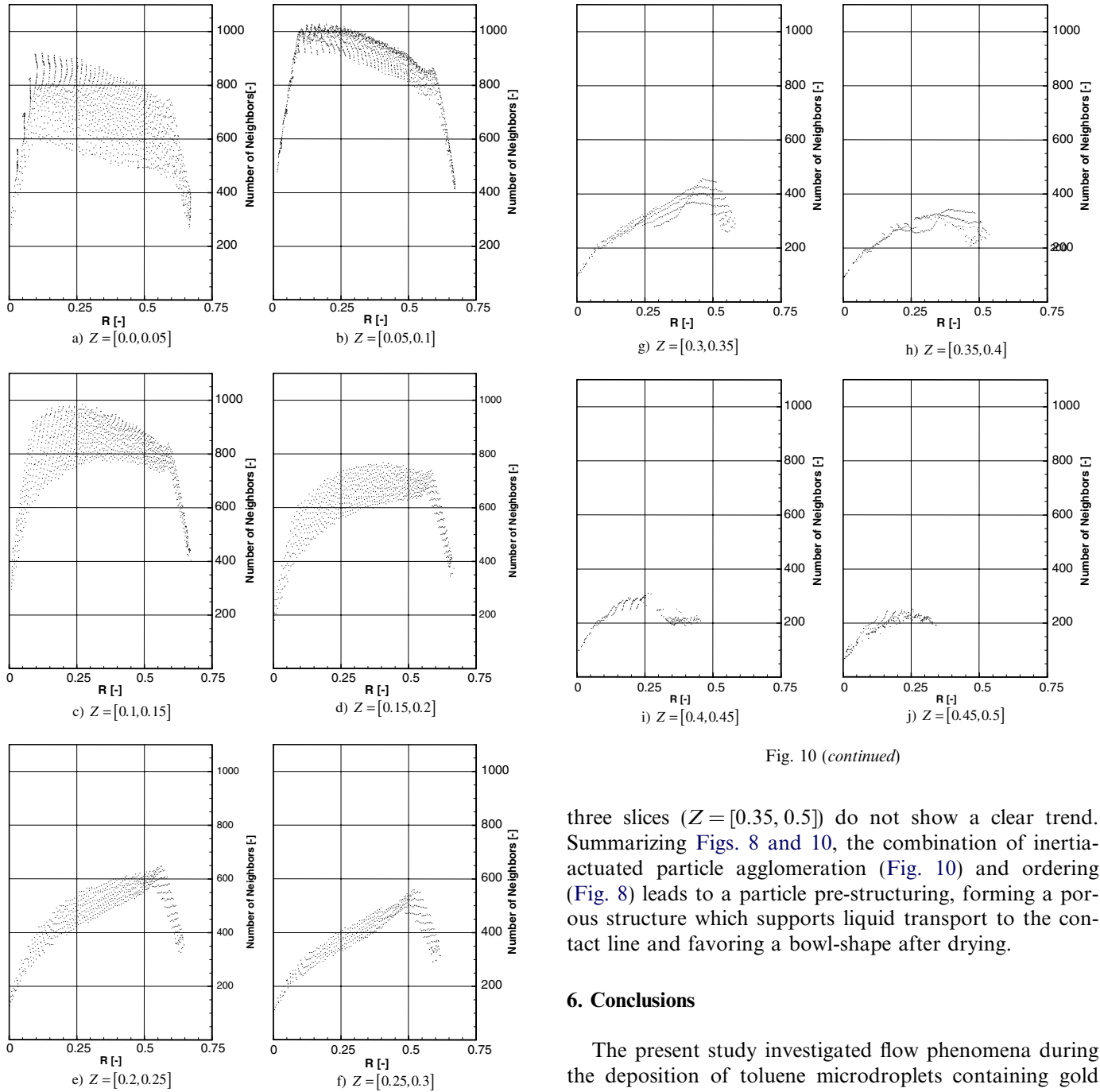
Fig. 10. Number of neighbor particles within cutoff radius at time $\tau = 7.0$ Shown are slices in radial direction of $\Delta Z = 0.05$ width starting from $Z = 0.0$ to $Z = 0.5$.

the corresponding computational particles are simulated (axis-symmetric domain). Thus, the small number of neighbors on the symmetry axis has no physical meaning. Particles at $R = 0.1$ and $Z = [0.05, 0.1]$ have the most neighbors, which is due to the particle agglomeration caused by the dynamic impact process. Interesting is the local maximum ($Z = [0, 0.2]$), respectively, global maximum ($Z = [0.2, 0.35]$) of neighbors in vicinity of the free surface. The latter slices (slice 5–7) resemble the bowl shape, whereas the last

three slices ($Z = [0.35, 0.5]$) do not show a clear trend. Summarizing Figs. 8 and 10, the combination of inertia-actuated particle agglomeration (Fig. 10) and ordering (Fig. 8) leads to a particle pre-structuring, forming a porous structure which supports liquid transport to the contact line and favoring a bowl-shape after drying.

6. Conclusions

The present study investigated flow phenomena during the deposition of toluene microdroplets containing gold nanoparticles on flat substrates under ambient conditions. Special attention was assigned to the dynamic aspects of the problem such as wetting and particle motion in the dilute limit. Experiments conducted with a high-speed camera were used to calibrate a numerical model providing additional insight in the particle motion and structure within the liquid. Spreading was shown to be reduced up to about 30% by the presence of particles which was attributed to the enhancement of viscosity, contact line friction and liquid–vapor interfacial tension. It was seen that the deviation from the case utilizing pure liquid originates predominantly from the initial inertia-dominated spreading regime, suggesting shear-thickening effects. Two wetting models based on the uncompensated Young force at the contact line as driving

mechanism for wetting were compared with each other. The incorporated particle model predicts segregation between solvent and particles due the specific flow pattern during oscillatory recoiling stages and a pre-structuring of the particles within a region in the substrate proximity. It is suggested that this mechanism can add to previously identified effects, namely thermocapillarity and evaporation, leading to the characteristic trough shape developing during the drying of colloidal suspension droplets.

Acknowledgements

References

Attinger, D., Zhao, Z., Poulikakos, D., 2000. An experimental study of molten microdroplet surface deposition and solidification: transient behavior and wetting angle dynamics. J. Heat Transfer 122, 544–556.

Aussillous, P., Quere, D., 2001. Liquid marbles. Nature 411, 924–927.

Bieri, N.R., Chung, J., Haferl, S.E., Poulikakos, D., Grigoropoulos, C.P., 2003. Microstructuring by printing and laser curing of nanoparticle solutions. Appl. Phys. Lett. 82, 3529–3531.

Blake, T.D., Haynes, J.M., 1969. Kinetics of liquid/liquid displacement. J. Colloid Interf. Sci. 30, 421–423.

Brady, J.F., 2001. Computer simulation of viscous suspensions. Chem. Eng. Sci. 56, 2921–2926.

Brenner, H., 1961. The slow motion of a sphere through a viscous fluid towards a plane surface. Chem. Eng. Sci. 16, 242–251.

Chorin, A.J., 1997. A numerical method for solving incompressible viscous flow problems (Reprint J. Comp. Phys. 2 (1967), 12–26). J. Comp. Phys. 135, 118–125.

Chung, J., Ko, S., Bieri, N.R., Grigoropoulos, C.P., Poulikakos, D., 2003. Laser Curing of Gold Nanoparticle Inks. In: IMECE 2003, Washington, DC.

Chung, J.W., Ko, S.W., Bieri, N.R., Grigoropoulos, C.P., Poulikakos, D., 2004. Conductor microstructures by laser curing of printed gold nanoparticle ink. Appl. Phys. Lett. 84, 801–803.

Deegan, R.D., Bakajin, O., Dupont, T.F., Huber, G., Nagel, S.R., Witten, T.A., 1997. Capillary flow as the cause of ring stains from dried liquid drops. Nature 389, 827–829.

De Gennes, P., 1985. Wetting: statics and dynamics. Rev. Mod. Phys. 57, 827–863.

Dietzel, M., Haferl, S., Ventikos, Y., Poulikakos, D., 2003. Marangoni and variable viscosity phenomena in picoliter size solder droplet deposition. J. Heat Transfer 125, 365–376.

Dietzel, M., Poulikakos, D., 2003. Marangoni and temperature dependent wetting phenomena in picoliter size solder droplet deposition. In: Proceedings of the Ninth International Conference on Liquid Atomization and Spray System – ICLASS 2003, Sorrento, Italy.

Dussan, E.B., Davis, S.H., 1974. Motion of a fluid–fluid interface along a solid-surface. J. Fluid Mech. 65, 71–96.

Egry, I., 1993. On the relation between surface-tension and viscosity for liquid-metals. Scrip. Metall. Mater. 28, 1273–1276.

Elghobashi, S., Truesdell, G.C., 1992. Direct simulation of particle dispersion in a decaying isotropic turbulence. J. Fluid Mech. 242, 655–700.

Fuller, S.B., Wilhelm, E.J., Jacobson, J.A., 2002. Ink-jet printed nanoparticle microelectromechanical systems. J. MEMS 11, 54–60.

Goedel, W.A., 2003. A simple theory of particle-assisted wetting. Europhys. Lett. 62, 607–613.

Haferl, S., Poulikakos, D., 2002. Transport and solidification phenomena in molten microdroplet pileup. J. Appl. Phys. 92, 1675–1689.

Haferl, S., Poulikakos, D., 2003. Experimental investigation of the transient impact fluid dynamics and solidification of a molten microdroplet pile-up. Int. J. Heat Mass Transfer 46, 535–550.

Hinds, W.C., 1998. Aerosol Technology: Properties, Behavior and Measurement of Airborne Particles. John Wiley & Sons, Inc.

Krieger, I.M., Dougherty, T.J., 1959. A mechanism for non-Newtonian flow in suspensions of rigid spheres. Trans. Soc. Rheol. 3, 137–152.

Landau, L.D., Lifshitz, E.M., 1959. Fluid Mechanics. Pergamon Press.

Maenosono, S., Dushkin, C.D., Saita, S., Yamaguchi, Y., 1999. Growth of a semiconductor nanoparticle ring during the drying of a suspension droplet. Langmuir 15, 957–965.

Maier, C., Aus Der Wiesche, S., Hofer, E.P., 2000. Impact of microdrops on solid surfaces for DNA-synthesis. In: MSM 2000 International Conference on Modeling and Simulation of Microsystems, San Diego.

Maxey, M.R., Riley, J.J., 1983. Equation of motion for a small rigid sphere in a nonuniform flow. Phys. Fluids 26, 883–889.

Mewis, J., Vermant, J., 2000. Rheology of sterically stabilized dispersions and lattices. Prog. Org. Coat. 40, 111–117.

Nesic, S., Vodnik, J., 1991. Kinetics of droplet evaporation. Chem. Eng. Sci. 46, 527–537.

Quemada, D., 1977. Rheology of concentrated disperse systems and minimum energy–dissipation principle. 1. Viscosity–concentration relationship. Rheo. Acta 16, 82–94.

Sun, Y.J., Walker, G.C., 2002. Two-dimensional self-assembly of latex particles in wetting films on patterned polymer surfaces. J. Phys. Chem. B 106, 2217–2223.

Tseng, W.J., Lin, K.C., 2003. Rheology and colloidal structure of aqueous TiO_2 nanoparticle suspensions. Mater. Sci. Eng. A 355, 186–192.

Waldvogel, J.M., 1995. Transport Phenomena and Solidification in Picoliter Solder Droplet Deposition. Ph.D. Thesis, Mechanical Engineering, University of Illinois at Chicago.

Yarin, A.L., Weiss, D.A., 1995. Impact of drops on solid-surfaces – self-similar capillary waves, and splashing as a new-type of kinematic discontinuity. J. Fluid Mech. 283, 141–173.